Correlations Between Structural and Magnetic Properties of Co$_2$FeSi Heusler-Alloy Thin Films

Weihua Zhu,[1] Di Wu,[1] Bingcheng Zhao,[1] Zhendong Zhu,[1] Xiaodi Yang,[2] Zongzhi Zhang,[1,*] and Q. Y. Jin[1]

[1]*Department of Optical Science and Engineering, Key Laboratory of Micro and Nano Photonic Structures*
(Ministry of Education), and Shanghai Ultra-Precision Optical Manufacturing Engineering Center,
Fudan University, Shanghai 200433, China
[2]*Laboratory of Advanced Materials, Fudan University, Shanghai 200438, China*

The structural and magnetic properties are the most important parameters for practical applications of Co-based Heusler alloys. The correlations between the crystallization degree, chemical order, magnetic coercivity, saturation magnetization (M_S), and in-plane magnetic anisotropies are systematically investigated for Co$_2$FeSi (CFS) films fabricated at different temperatures (T_S). XRD shows that the CFS layer changes progressively from a disordered crystal structure into a chemically disordered $A2$ structure and further into a chemically ordered $B2$ and even $L2_1$ structures when increasing T_S up to 480 °C. Meanwhile, the static angular remanence magnetization curves show a clear transition of magnetic anisotropy from twofold to fourfold symmetry, due to the competition effect between the uniaxial anisotropy field H_U and biaxial anisotropy field H_B. The H_U value is found to be weakly dependent on T_S, while H_B shows a continuous enhancement at $T_S > 300$ °C, implying that the enhancement of the $L2_1$ ordering degree would not weaken the biaxial anisotropy. The varying trend of H_B is similar to M_S, which can be respectively attributed to the improved crystal structure and chemical order. The anisotropic fields and their variation behaviors determined by a vibrating sample magnetometer are highly consistent with the results by a time-resolved magneto-optical Kerr effect study. Our findings provide a better understanding of the structural ordering and magnetic anisotropy, which will be helpful for designing advanced spintronic devices.

I. INTRODUCTION

Full-Heusler alloys (FHAs) are attracting considerable attention due to their great advantages including lattice match with the III-V semiconductors, half-metallic band structure with high spin polarization P, and reduced magnetic damping constant α [1–4]. The compounds are usually described by the formula X_2YZ, where X and Y are transition metals and Z is a main group element. Among the various types of FHAs, it has been predicted that the Co-based FHAs, such as Co$_2$FeSi (CFS) alloy, owns a very high Curie temperature $T_C \sim 1100$ K and a quite large magnetic moment up to $6\mu_B$ [5,6]. With these merits, the FHAs as spin source materials are highly appropriate for practical applications in spintronic devices [7]. The FHA-based magnetic tunnel junctions (MTJs) are very successful and are of great technological interest for developing spin-transfer-torque magnetic random access memory (STT MRAM) devices. Very large tunneling magnetoresistance (TMR) signals up to 429% at room temperature (RT) are reported in MTJs by using the FHA layer as the free and reference magnetic electrodes [8–10]. Moreover, the current–perpendicular-to-plane (CPP) spin-valve devices with a highly spin-polarized electrode of FHAs have also attracted great attention [11,12]. A rather high

giant MR ratio of 58% at RT is demonstrated in Co$_2$Fe$_x$Mn$_{1-x}$Si/Ag/Co$_2$Fe$_x$Mn$_{1-x}$Si CPP devices [13], and the MR ratio and associated resistance-area product satisfy the requirements for a Tbit/in^2 hard-disk-drive read head. In addition, the half-metallic FHAs allow the injection of highly spin-polarized current into a semiconductor through its spin-up channel [14–16], and the injected current is fully spin polarized, which makes them ideal candidates for spin contacts on semiconductors and for developing devices with new functions as well.

It is known that developing STT MRAM with high performance requires the ferromagnetic electrode material with improved parameters of high spin polarization and low magnetic damping for efficient STT switching at a reduced current density and large TMR signal [17,18]. Although high P and low α have been theoretically predicted for FHAs due to the lack of minority spin density of states at the Fermi level, the experimentally measured results are not as good as expected. For the successful implementation of FHA films into next-generation magnetic storage, it is of key importance to optimize the crystal structure and material properties. As we know, the advanced magnetic properties of CFS films are closely related to the chemical order [19,20], which are sensitive to the deposition condition, atomic composition, and adjacent layers. The CFS film fabricated at low temperatures usually has a disordered $A2$ phase, with atoms randomly placed in a body-centered

*zzzhang@fudan.edu.cn

cubic lattice. The formation of chemically ordered $B2$ and $L2_1$ structures usually requires a high growth temperature and/or postannealing treatment [19,21–23]. In most cases, multiple structure types may coexist. The existence of disordered phases may worsen the magnetic properties. It is found that the damping parameter decreases with the increase of atomic ordering [24]. And among these three structure types categorized by occupation of the available atomic sites, only the chemically ordered structures showed half-metallic behavior [24,25]. Although there are quite a few works performed on the structural and magnetic properties of the FHA films, the exact relationship and underlying mechanism still remain unclear. The saturation magnetization (M_S) and spin polarization of Co-based FHAs increase simultaneously with the increase of the chemical ordering degree [26,27], while some other researchers observed a reduction of M_S which may be related to the diffusion of impurity atoms from the buffer layer [28–30]. Apart from the spin polarization and saturation magnetization, other magnetic properties such as magnetic anisotropy are also very important and should be carefully characterized and controlled. It is expected that the cubic-crystal structure should present an in-plane biaxial anisotropy for the (001) epitaxial films. However, an additional in-plane uniaxial magnetic anisotropy has often been reported for the FHA films grown on various single-crystalline substrates [29,31–36]. Moreover, quite different and even opposite varying behaviors are observed for the uniaxial and biaxial magnetic anisotropies as the annealing temperature increases [21,22,37–39]. A strong reduction of biaxial anisotropy is found and attributed to the increasing fraction of the $L2_1$ phase [21,22,38,39]. However, the authors do not exclude the origin from an annealing-induced atomic diffusion effect. The magnetic anisotropy not only determines the magnetization-switching behaviors but affects the magnetic damping constant and device thermal stability as well. Moreover, the coexistence of uniaxial and biaxial magnetic anisotropies can complicate the magnetization-switching process, which should be clarified for practical applications. As we can see, the performances of spintronic devices rely significantly on the structural and magnetic properties of the full-Heusler-alloy films.

In order to achieve effective control of the material properties for designing appropriate spintronic devices, it is of key importance to acquire a general picture on the correlations between the sample structure and magnetic properties. Considering the chemical order is directly correlated to the atom arrangement, tailoring the lattice site occupation of the CFS alloy provides an efficient way to control the material properties. Therefore, in this work we perform a detailed study on the CFS thin films grown on MgO(001) single-crystalline substrates. In order to exclude the influence of atomic diffusion on magnetic properties, only the CFS layer is *in situ* heated at various substrate temperatures (T_S), while the Ta top layer is deposited

at RT. The crystal structure and chemical order of CFS layers are characterized by XRD, and the T_S-dependent magnetic properties are deduced according to the static and dynamic magnetization measurements.

II. EXPERIMENT

All the samples, in a structure of CFS (15 nm)/Ta(7 nm), are fabricated on MgO(001) single-crystalline substrates by dc magnetron sputtering under a base pressure better than 3.0×10^{-8} Torr. The deposition rate is fixed as 0.10 Å/s for the CFS layer and 0.52 Å/s for the Ta cap layer, respectively. The CFS layer is sputtered from an alloy target with a stoichiometric composition of $Co_{50}Fe_{25}Si_{25}$ under an Ar pressure of 4 mTorr. The top Ta layer is used to protect the CFS layer against oxidation. In order to form differently ordered phases, the CFS layers are deposited at various substrate temperatures of $T_S = 200$, 300, 350, 400, and 480 °C, and they are further *in situ* annealed at the same temperature for 10 min prior to the Ta-layer deposition. Then, the Ta cap layer is sputtered after the CFS layer is naturally cooled to RT.

The film crystallographic texture is examined by a high-resolution four-circle x-ray diffractometer with Cu $K\alpha$ radiation. A vibrating sample magnetometer (VSM) is utilized to measure the magnetic hysteresis loops and angular remanence magnetization (ARM) curves. The dynamic magnetic properties are acquired by a pump-probe system based on the time-resolved magneto-optical Kerr effect (TRMOKE). The TRMOKE measurements are achieved using a pulsed Ti:sapphire laser with a central wavelength of 800 nm, a pulse duration of 150 fs, and a repetition rate of 1000 Hz [40]. An intense pump pulse beam with a fluence of approximately 7.0 mJ/cm² is used to excite the magnetization precession behavior, and the transient MOKE signal is detected by a weak probe pulse of approximately 0.6 mJ/cm² which is time delayed with respect to the pump beam. The pump and probe laser beams are at almost perpendicular incidence, with spot diameters of about 4.0 and 0.2 mm, respectively. During the TRMOKE measurement, an external magnetic field H is applied at an angle of $\theta_H = 71°$ in order to drive the magnetization orientation away from the in-plane easy axis. Note that all the measurements are conducted at RT.

III. STRUCTURAL CHARACTERIZATION

As we know, the Co_2FeSi Heusler-alloy crystal usually includes three kinds of atomic structure, i.e., $L2_1$, $B2$, and $A2$ with different chemical ordering degrees. Figure 1(a) presents the highly ordered $L2_1$ structure (space group no. 216: $F\text{-}43m$), the two Co atoms occupy the (0, 0, 0) and (0.5, 0.5, 0.5) positions, the Fe atom occupies the (0.25, 0.25, 0.25) position, and the Si atom occupies the (0.75, 0.75, 0.75) position. The cubic $L2_1$ structure cell consists of four interpenetrating face-centered cubic (fcc) sublattices,
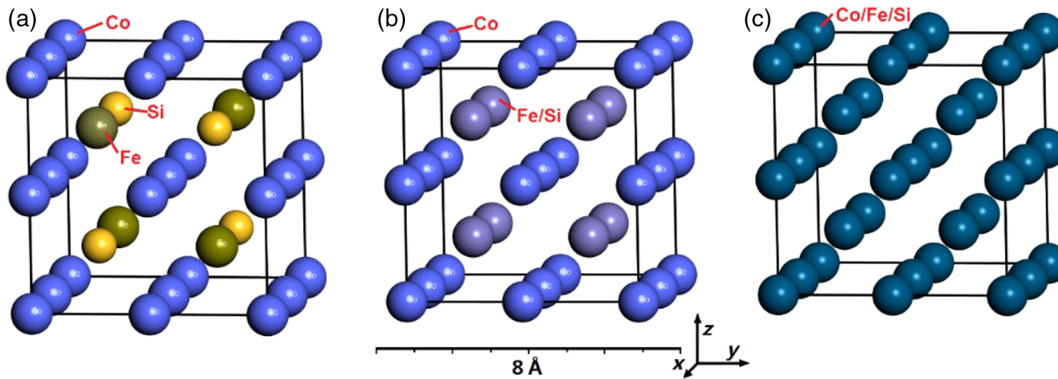
FIG. 1. The ordered $L2_1$ structure (a) and the disorder $B2$ structure (b) and $A2$ structure (c).

two of which are equally occupied by Co, and the rest two are occupied by Fe and Si. The two Co-site fcc sublattices form a simple cubic sublattice structure, in which the Fe and Si atoms are alternatingly located in the center sites. If the Fe and Si atomic sites are randomly occupied, the ordering degree decreases and the $L2_1$ structure changes to the $B2$ structure (space group no. 225: $Fm\text{-}3m$), as shown in Fig. 1(b). Figure 1(c) displays the completely disordered $A2$ structure, in which all the atomic sites are occupied randomly. Nearly all the magnetic properties of the CFS films are related to the crystalline quality and atomic site occupation [41], which can be characterized by the XRD measurements. The (111) superlattice diffraction peak indicates the presence of ordered $L2_1$ structure, while the (002) superlattice peak is a main characteristic of $B2$ structure.

Figure 2(a) shows the $\theta - 2\theta$ patterns for CFS films grown at various substrate temperatures. For the samples of $T_S = 300\,°C$ or lower, apart from the strong (002) peak arising from the MgO substrate, no other diffraction peaks can be detected, which suggests that the samples deposited at low temperatures have a disordered crystal structure, probably due to the presence of defects created in the lattice by energetic atom bombardment during sputtering. A weak (004) peak appears at $T_S = 350\,°C$, implying that the CFS film with structure disorder starts to crystallize in the chemically disordered $A2$ phase. As T_S is further increased up to $400\,°C$ and above, the diffraction peaks of both CFS (002) and CFS (004) can be observed, indicating the CFS films are (001) oriented in the out-of-plane direction and have at least a $B2$ structure. The CFS peak intensity increases considerably with the increase of T_S, as the result of reduced lattice defects and hence improved crystal structure. From the diffraction patterns, we can estimate the CFS grain size D by using the Scherrer equation [42], $D = [(k\lambda)/\beta\cos\theta]$, where k of approximately 0.89 is a dimensionless shape factor, λ is the x-ray wavelength of 0.154 nm, β is the full width at half maximum of the diffraction peaks, and θ here is the diffraction angle of the CFS (004) peak (in units of degree). As expected, increasing the substrate temperature can lead to obvious crystallization and grain growth; the calculated grain sizes are

approximately 7.4, 12.5, and 13.8 nm for $T_S = 350, 400,$ and $480\,°C$, respectively.

In order to clarify the epitaxial relationship and chemical order of CFS films in the atomic level, Φ scan measurements are performed for the CFS films of $T_S = 350, 400,$ and $480\,°C$. Figures 2(b) and 2(c) show the patterns of CFS $\langle 220 \rangle$ obtained at $2\theta = 45.48°$, $\psi = 45.20°$ and CFS $\langle 111 \rangle$ at $2\theta = 27.36°$, $\psi = 54.71°$, respectively. Here Φ corresponds to the in-plane rotation angle and ψ the tilt angle [43], and $\Phi = 0$ is defined as the direction of the MgO [110]. Apparently, the four $\langle 220 \rangle$ diffraction peaks shown in Fig. 2(b) are separated periodically with an angle difference of 90°, indicating that the CFS film has a fourfold symmetry. From the relative peak positions of CFS (220) in the Φ scan patterns, we can determine
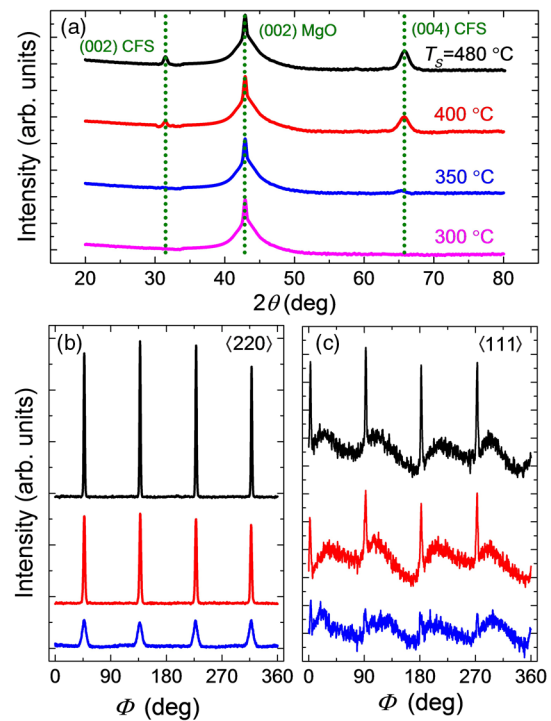

FIG. 2. XRD patterns of the (a) $\theta - 2\theta$ scan, (b) Φ scan for the CFS (220) diffraction peaks, and (c) Φ scan for CFS (111) diffraction peaks.

TABLE I. The values of part samples for S_{B2} and S_{L21}.

T_S (°C)	S_{B2} (%)	S_{L21} (%)
350	0	0
400	73.6	46.7
480	82.7	56.9

that the CFS films of $T_S \geq 350\,°C$ are epitaxially grown on the MgO substrates, with an epitaxial relation of MgO(001)[100]‖CFS(001)[110]. The peak intensity of all the diffraction lines is decreasing with T_S, due to the increased disorder and poor epitaxial growth of the CFS crystal at lower substrate temperatures. Figure 2(c) shows the evolution of CFS $\langle 111 \rangle$ superlattice diffraction peaks, verifying the presence of an atomically ordered $L2_1$ phase at $T_S > 350\,°C$. Note that the corresponding (220) and (111) diffraction peaks are separated by 45°, coinciding well with the crystal structure of CFS.

The parameters of chemical ordering degree, S_{L21} for the $L2_1$ phase and S_{B2} for the $B2$ phase, can be evaluated by the relative peak intensities according to the extended Webster model [19,44],

$$\frac{I_{200}}{I_{400}} = S_{B2}^2 \frac{I_{200}^{\text{full-order}}}{I_{400}^{\text{full-order}}},$$

$$\frac{I_{111}}{I_{220}} = \left(S_{L2_1} \cdot \frac{3 - S_{B2}^2}{2} \right) \frac{I_{111}^{\text{full-order}}}{I_{220}^{\text{full-order}}}, \qquad (3.1)$$

where I_{hkl} and $I_{hkl}^{\text{full-order}}$ are the experimentally obtained diffraction intensity of the CFS hkl plane and the theoretically calculated diffraction intensity of the fully $L2_1$ ordered CFS alloys, respectively. According to Ref. [19], the parameter S_{B2} for the full-Heusler X_2YZ alloy of Co_2FeSi represents the random occupation between X and Y (or Z) sites. In contrast, the fraction of Y atoms on the Z sites is generally used to evaluate the $L2_1$ ordering degree S_{L21}. As a result, for the completely disordered $A2$ crystal structure, both order parameters of S_{B2} and S_{L21} are zero. The S_{B2} value is 100% as long as the X sites are orderly occupied by Co atoms, no matter whether the Y and Z sites are random or not. It has been pointed out that the S_{L21} value depends on the ordering degree of $B2$, which increases with S_{B2} [19]. The calculated ordering parameters are listed in Table I. Clearly, S_{L21} and S_{B2} increase with the substrate temperature, and a higher substrate temperature is advantageous for the transformation of $B2$ into $L2_1$ structure. From these results, it can be concluded that the samples of $T_S = 300\,°C$ and below have a disordered crystal structure. As T_S is $350\,°C$, the chemically disordered $A2$ crystal structure forms, which gradually evolves towards a partially chemically ordered $B2$ and completely ordered $L2_1$ structure when further increasing the substrate temperature. As shown in the next sections, the evolutions of the sample crystal structure and chemical ordering degree are well correlated with the variation of magnetic properties.

IV. INVESTIGATIONS OF MAGNETIC PROPERTIES

A. Static magnetic measurements by VSM

The magnetic hysteresis loops and ARM curves are measured by VSM for all the samples, with an in-plane magnetic field applied along various orientations. For the convenience of data analyses, we build up a polar coordinate system. As shown in Fig. 3(a), the z axis is perpendicular to the sample plane, and the x and y axes are, respectively, parallel to the [110] and [1$\bar{1}$0] crystallographic directions of the CFS layer. The φ_M (or φ_H) is defined as the in-plane angle of magnetization **M** (or applied magnetic field **H**) with respect to the x axis, while θ_M (or θ_H) is the corresponding out-of-plane angle between **M** (or **H**) and the z axis. From the VSM measurements, we know that there are two kinds of in-plane magnetic anisotropies for our CFS films: a biaxial magnetic anisotropy with two easy axes along the [110] (x axis) and [1$\bar{1}$0] (y axis) directions and a uniaxial anisotropy with an easy axis along the [110] direction.

Based on the polar coordinate system, the total free energy density E of our CFS films, which includes the Zeeman energy, demagnetizing energy, and anisotropy energy, can be given as [23,45]

$$E = E_{\text{Zeeman}} + E_{\text{demagn}} + E_{\text{aniso}}$$
$$= -M_S H[\sin\theta_M \sin\theta_H \cos(\varphi_H - \varphi_M) + \cos\theta_M \cos\theta_H]$$
$$\quad - 2\pi M_S^2 \sin^2\theta_M + \frac{1}{4} K_B \sin^2(2\varphi_M)\sin^4\theta_M$$
$$\quad + K_U \sin^2\varphi_M \sin^2\theta_M + K_\perp \sin^2\theta_M, \qquad (4.1)$$

where K_B represents the in-plane biaxial magnetic anisotropy constant, K_U the in-plane uniaxial magnetic anisotropy constant, and $K_\perp$ the out-of-plane uniaxial magnetic anisotropy constant. Here, we define $H_U = 2K_U/M_S$ and $H_B = 4K_B/M_S$ as the in-plane uniaxial and biaxial magnetic anisotropy fields, respectively, and $H_\perp = 2K_\perp/M_S$ as the out-of-plane uniaxial magnetic anisotropy field. According to the Stoner-Wohlfarth coherent rotation model [46], the equilibrium position of magnetization can be determined from the minimum free energy density:
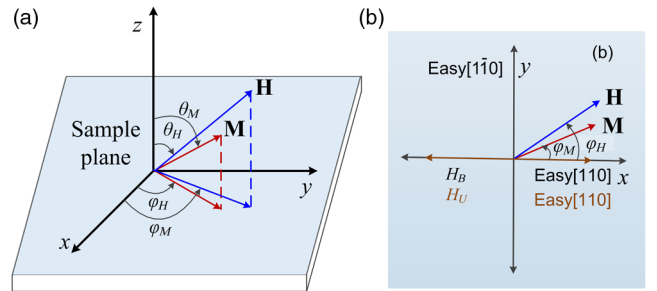

FIG. 3. The polar coordinate system (a) and its in-plane geometry (b) for magnetic measurement and data analyses.

$$\frac{\partial E}{\partial \theta_M} = -M_S H[\cos\theta_M \sin\theta_H \cos(\varphi_H - \varphi_M) - \sin\theta_M \cos\theta_H]$$

$$- 2\pi M_S^2 \sin(2\theta_M) + \frac{K_B}{2}\sin^2(2\varphi_M)\sin^2\theta_M \sin(2\theta_M)$$

$$+ K_U \sin^2\varphi_M \sin(2\theta_M) + K_\perp \sin(2\theta_M) = 0, \qquad (4.2)$$

$$\frac{\partial E}{\partial \varphi_M} = -M_S H[\sin\theta_M \sin\theta_H \sin(\varphi_H - \varphi_M)]$$

$$+ \frac{K_B}{2}\sin^4\theta_M \sin(4\varphi_M) + K_U \sin^2\theta_M \sin(2\varphi_M) = 0.$$

$$(4.3)$$

As the CFS samples have in-plane magnetic anisotropy and the external magnetic field is applied in plane during the VSM measurement, the magnetization should also stay in the film plane [see the corresponding in-plane geometry depicted in Fig. 3(b)]. In this case, both θ_M and θ_H are equal to $\pi/2$, and the equilibrium position equation of in-plane magnetization can be simplified as

$$\frac{K_B}{2}\sin(4\varphi_M) + K_U \sin(2\varphi_M) = M_S H \sin(\varphi_H - \varphi_M). \qquad (4.4)$$

According to this equation, the magnetic anisotropy constants can be deduced by fitting the field dependence of hard-axis magnetization curves. Meanwhile, if we set the applied field H in Eq. (4.4) as zero, we can get the angular dependence relation of remanent magnetization:

$$\frac{K_B}{2}\sin(4\varphi_M) + K_U \sin(2\varphi_M) = 0. \qquad (4.5)$$

As a result, if the fitted magnetic anisotropy constants are input into Eq. (4.5), the corresponding ARM curves can be simulated. In the following, we show the static magnetic properties and related data analyses based on the above equations of (4.4) and (4.5).

Figure 4(a) shows the normalized in-plane magnetic hysteresis loops for CFS films grown at different temperatures. The external field is applied along the main crystallographic directions of [110], [100], or [1$\bar{1}$0], i.e., $\varphi_H = 0, 45°$, and $90°$, respectively. Clearly, the loop shape varies considerably with the substrate temperature and field orientation. For the sample deposited at 200 °C, from the weak difference in remanent magnetization, we are able to recognize that the [110] and [1$\bar{1}$0] directions are slightly inequivalent. The sample has a weak in-plane uniaxial anisotropy, with the easy axis along the [110] direction and a hard axis along the [1$\bar{1}$0] direction. As T_S increases, the remanences of the [110] and [1$\bar{1}$0] directions both increase; they eventually go to the same value of 1 at $T_S \geq 350$ °C. According to the structural analyses, it infers that a biaxial magnetic anisotropy develops with the improved CFS crystal structure at higher T_S, giving rise to the two equivalent easy axes and the transformation of the hard-axis direction from [1$\bar{1}$0] to [100].
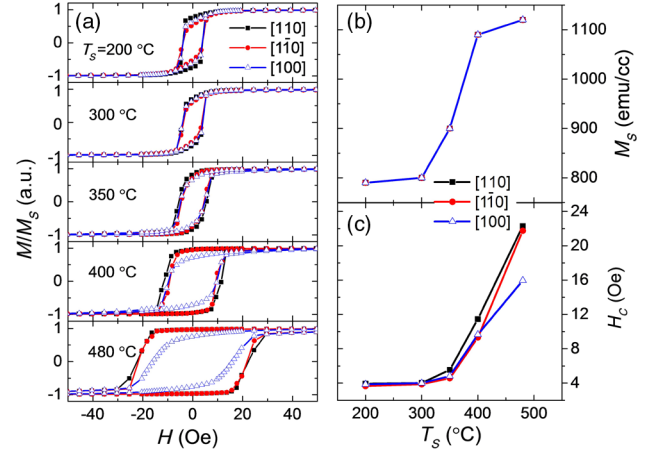

FIG. 4. Magnetic properties obtained by VSM measurements. (a) Magnetic hysteresis loops of CFS films grown at different T_S, with magnetic field H applied parallel to the main crystallographic axes of [110], [1$\bar{1}$0], and [100]. (b) The saturation magnetization M_S and (c) magnetic coercivity H_C as a function of T_S for the three kinds of field orientation.

The saturation magnetization M_S and magnetic coercivity H_C are derived from the hysteresis loops and summarized in Figs. 4(b) and 4(c), respectively, as a function of T_S. Interestingly, M_S and H_C display a very similar varying trend. Both of them keep nearly unchanged at $T_S \leq 300$ °C; afterwards, they start to rise considerably. The maximum of M_S is 1120 emu/cm^3, which is slightly lower than the ideal bulk value due to the incompletely chemical ordering of $B2$ or $L2_1$ structure [47]. The increasing trend of M_S is in good agreement with other studies and is believed to result from the improved chemical ordering between Co and Fe sites [37,48]. Note that, at $T_S < 350$ °C, the H_C values are rather small and nearly equal for the three different field directions. However, with increasing the substrate temperature, the H_C of the [110] and [1$\bar{1}$0] directions exhibits a similar faster rising rate than that of the [100] direction. The observed increase in H_C is mainly due to the enhanced biaxial magnetic anisotropy [49]. In addition, the improved crystalline quality may also play some role. As we know from the XRD results, with increasing T_S the crystal structure is improved due to the reduction of lattice defects or imperfections. In this case, the antimagnetized nuclei would not be easy to form, which will lead to the increase of H_C as well. Note that in Ref. [20] the authors reported a decreasing behavior of H_C with annealing temperature for their Co$_2$FeAl film; we consider the opposite variation tendency arises largely from the large film thickness of 55 nm.

In order to clearly understand the evolution of magnetic anisotropy and clarify the effect of substrate heating, we measure the angular remanence magnetization curves. The remanence ratio M_r/M_S is shown in Fig. 5 as a function of angle φ_H with respect to the [110] direction. Clearly, the ARM curves of $T_S = 200$ and 300 °C show uniaxial
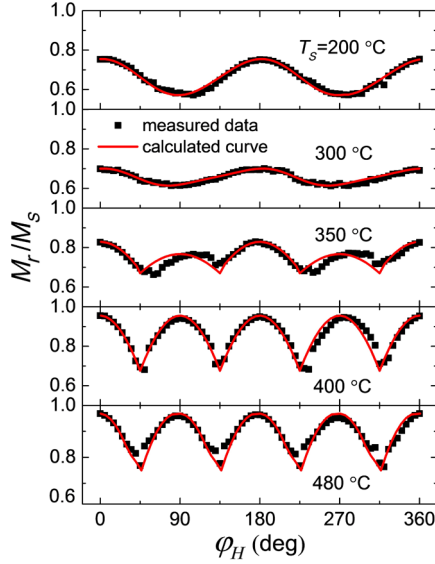
FIG. 5. The ARM curves for CFS films grown at different temperatures. The black points represent the experimental data, while the red lines are from the numerical calculation.
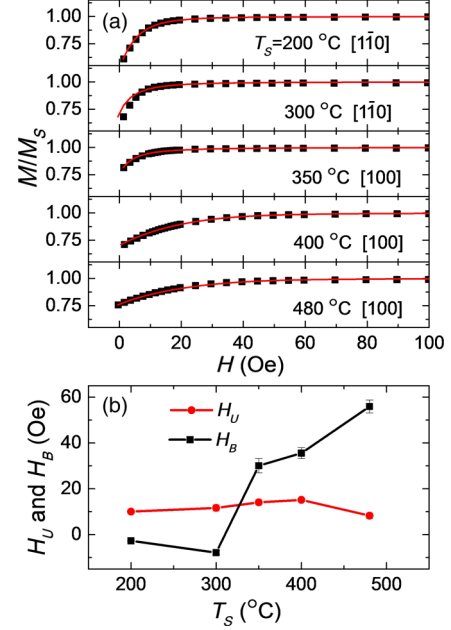

FIG. 6. (a) The experimental data points and fitted lines for the magnetic curves measured along the corresponding hard-axis orientation. (b) The in-plane uniaxial magnetic anisotropy field H_U and biaxial magnetic anisotropy field H_B versus T_S, calculated according to the Stoner-Wohlfarth model.

magnetic anisotropy with twofold symmetry. The maximum remanence ratio at $\varphi_H = 0$ and 180° denotes that the uniaxial easy axis is parallel to the [110] direction, and the minimum ratio at $\varphi_H = 90°$ implies that the hard-axis direction is along the [1$\bar{1}$0] direction. With the increase of T_S, the curves gradually evolve from a twofold to fourfold rotational symmetry, implying the emergence of a biaxial anisotropy. In addition, the minimum remanence ratio (hard axis) moves towards smaller φ_H, i.e., the direction of [100]. The additional remanence peak occurs not at $\varphi_H = 90°$ (i.e., the [1$\bar{1}$0] direction) for $T_S = 350\,°C$, which suggests the easy axes of biaxial anisotropy are not yet strictly along the [110] and [1$\bar{1}$0] directions. This is understandable, since the structural order of the CFS crystal is rather weak at such a low substrate temperature. When T_S is over 400 °C, the shape of the ARM curves is governed by the enhanced biaxial anisotropy, showing excellent fourfold symmetry with two equivalent easy axes along the [110] and [1$\bar{1}$0] directions. Meanwhile, the minimum remanence occurs at $\varphi_H = 45°$, indicating that the hard magnetic axis shifts to the [100] direction.

The quantitative values of uniaxial and biaxial magnetic anisotropy fields, H_U and H_B, respectively, can be numerically obtained by fitting the reversible part (from saturation field to zero) of the hard-axis magnetization loops, where the magnetization reversal can be treated as coherent rotation. Figure 6(a) shows the corresponding experimental data points and fitted reversible curves according to Eq. (4.4). The data points are taken from the magnetic loops of the [1$\bar{1}$0] direction for $T_S \leq 300\,°C$ and of the [100] direction for $T_S > 300\,°C$. Apparently, all the experimental data are well fitted by the solid lines, indicating that the hard-axis magnetization curve is basically a coherent

rotation process. Figure 6(b) shows the H_U and H_B values obtained from the numerical fitting. By using the fitted anisotropy fields and Eq. (4.5), the corresponding ARM curves can be calculated (the solid red lines in Fig. 5). It is found that, except for the case of 350 °C, the calculated ARM curves agree satisfactorily with the experimental data, revealing that the fitted H_U and H_B values are appropriate. As for the poor simulation of 350 °C, it should come from the fact that the used H_U and H_B values are obtained by fitting the magnetization curve of the [100] direction. However, from Fig. 5, we can see that the actual hard axis apparently deviates away from this orientation, which inevitably gives rise to improper anisotropic fields and hence the observed inconsistent simulation curve.

The fitted uniaxial magnetic anisotropy field H_U shown in Fig. 6(b) is rather small, showing a weak nonmonotonic dependence on the substrate temperature. The varying behavior is consistent with those of $Fe_{31}Co_{69}$ grown on (001) Ga [50] and Co_2FeAl on (001) MgO [21]. Up to now, no clear explanation has been given for the uniaxial anisotropy. It is reported that uniaxial magnetic anisotropy in some soft magnetic thin films may arise, because the process of atoms reaching the substrate is not isotropic during deposition at an oblique angle [51–53]. However, for our CFS films, the uniaxial anisotropy happens not due to this cause. For our sputtering machine, the substrate holder is rotated at a speed of 20 rpm during film deposition to ensure film uniformity, and no external magnetic field is applied in plane. As a result, we consider that the presence

of such weak uniaxial anisotropy in this study is most likely related to the symmetry breaking at the MgO/CFS interface due to the surface reconstruction or interface bonding effect [33,54]. Anisotropic relaxation of strains induced by the lattice mismatch may also play a role [32].

The different magnetization-switching behaviors and the transition from twofold to fourfold symmetry in ARM curves are a result of the competition effect between the uniaxial and biaxial magnetic anisotropies. In contrast to H_U, the biaxial magnetocrystalline anisotropy field H_B, which arises from the bulk crystal structure, displays a strong dependence on the substrate temperature. It is negligible at low T_S but increases rapidly and reaches nearly 60 Oe at $T_S = 480\,°C$. The increasing tendency of our H_B data is in accord with the result reported by Gabor *et al.* for MgO(001)/Co_2FeAl samples [37], which is ascribed to the improved crystal structure and enhanced in-plane biaxial strain. Interestingly, the T_S dependence of H_B is very similar to H_C shown in Fig. 4, from which we can get the information that the enhanced biaxial magnetocrystalline anisotropy governs the change of H_C. Accompanying the enhanced biaxial magnetic anisotropy, the ordering parameter S_{L2_1} increases as well when the substrate temperature is increasing, which suggests that the increasing amount of the $L2_1$ phase would not give rise to a reduction of H_B. As a result, we think that the observed decreasing trend of biaxial anisotropy with T_S by others [39] may not be associated with the ordering degree change of $L2_1$ phase. It is more likely caused by the interfacial diffusion of Cr atoms into the magnetic layer, since their full-Heusler films are *ex situ* annealed simultaneously with the adjacent nonmagnetic Cr buffer layer. One possible proof is that they observe a continuous reduction in M_S when increasing the annealing temperature, which is contrary to the increasing behavior of M_S of our CFS samples.

B. Dynamic magnetic measurements by TRMOKE

Ultrafast magnetization dynamics is measured by TRMOKE to verify the influence of T_S on the magnetic properties of CFS films. During the dynamic measurement, a magnetic field H is applied with a polar angle of $\theta_H = 71°$ and an azimuth angle φ_H corresponding to the magnetic hard-axis direction mentioned above, i.e., $\varphi_H = 90°$ for $T_S \leq 300\,°C$ and $45°$ for $T_S > 300\,°C$. The typical TRMOKE data points are displayed in Fig. 7(a) for the case of $H = 2$ kOe. Similar to many other magnetic thin films, the dynamic Kerr signal θ_k displays an ultrafast demagnetization and a subsequent magnetization precession process. The magnetization precession and damping part can be fitted by using the following sinusoidal equation [22,55]:

$$\theta_k = a + b\exp(t/t_0) + c\sin(2\pi f t + \varphi)\exp(-t/\tau), \quad (4.6)$$

where the first term is the background signal, the second term corresponds to the slow magnetization recovery
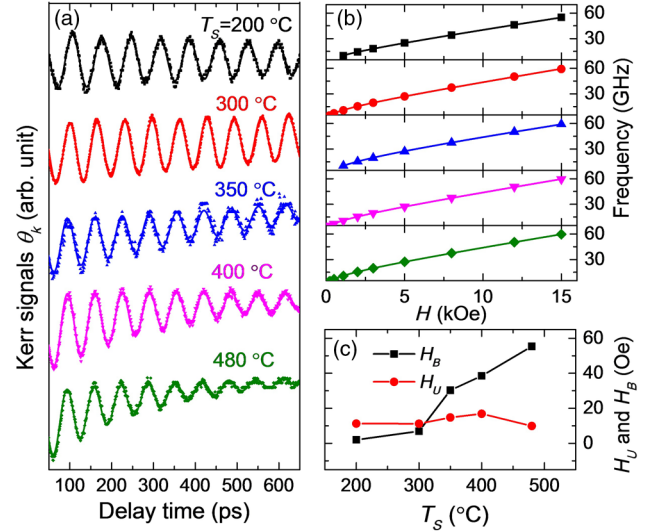

FIG. 7. (a) The laser-induced magnetization dynamic Kerr signals (symbols) measured at $H = 2$ kOe and the corresponding fitting curves (solid lines) for CFS films grown at different T_S. (b) The relationship between precession frequency f and the applied field H at various T_S. (c) The T_S dependences of H_U and H_B values obtained by fitting the curves shown in (b).

process, and the third term describes the uniform magnetization precession dynamics. The parameters of c, f, φ, and τ represent the precession amplitude, frequency, initial phase, and decay time of magnetization, respectively. The fitted frequency is plotted in Fig. 7(b) as a function of external magnetic field H for samples grown at different T_S, which is seen to increase almost linearly with the magnetic field H. It is known that the varying trend of such a field-dependent precession frequency is determined by the coaction of an external field and effective magnetic anisotropy fields. The field-dependent frequency curves in Fig. 7(b) are fitted by the following Kittel formula of the uniform precession mode [22]:

$$f = \frac{\gamma}{2\pi}\{[H\cos(\varphi_H - \varphi_M) + H_1]$$
$$\times [H\cos(\varphi_H - \varphi_M) + H_2]\}^{1/2}. \quad (4.7)$$

where $\gamma = \gamma_e g/2$ is the gyromagnetic ratio of the electron with $\gamma_e = 1.76 \times 10^7$ Hz/Oe and $g = 2.06$. H_1 and H_2 are, respectively, defined as

$$H_1 = 4\pi M_S - \frac{2K_\perp}{M_S} - \frac{K_B}{M_S}\sin^2(2\varphi_M) - \frac{2K_U}{M_S}\sin^2\varphi_M,$$

$$H_2 = \frac{2K_B}{M_S}\cos(4\varphi_M) + \frac{2K_U}{M_S}\cos(2\varphi_M). \quad (4.8)$$

Note that the experimental data are well fitted by the lines, implying that the magnetization precession behaves in a uniform precession mode. Figure 7(c) shows the in-plane uniaxial and biaxial anisotropy fields obtained from the

curve fitting in Fig. 7(b). Apparently, the values of H_U and H_B, as well as their varying trends, are very consistent with the results obtained by VSM measurements [Fig. 6(b)], further verifying the existence of a nearly invariable in-plane uniaxial anisotropy and a biaxial magnetic anisotropy which grows rapidly with the increase of T_S.

From the above structural and magnetic results, the evolutions of sample structure and magnetic anisotropies upon thermal heating, as well as their correlations, can be identified. As T_S is lower than 300 °C, the CFS films show a disordered crystal structure, where the biaxial anisotropy is negligible and the uniaxial magnetic anisotropy dominates. As T_S is increased to 350 °C, accompanying with the onset of the $A2$ phase, the biaxial anisotropy occurs. With a further increase of T_S, both the biaxial anisotropy and saturation magnetization increase significantly, which are, respectively, due to the improved crystal structure and chemical order. The increased biaxial anisotropy plays a dominant role in the magnetization-switching behaviors for CFS samples deposited at $T_S > 350$ °C.

V. CONCLUSIONS

In this paper, we present correlated analyses on the structure, magnetic coercivity, saturation magnetization, and in-plane magnetic anisotropies for CFS films grown at different T_S. XRD reveals that, with the increase of T_S, the CFS layer develops first from disordered crystal structure to disordered $A2$ structure and then to chemically ordered $B2$ and $L2_1$ structures. Accompanying the increased chemical order and saturation magnetization, a gradual transition from twofold to fourfold symmetry occurs in the ARM curves, which is ascribed to the competition effect between the in-plane uniaxial and biaxial magnetic anisotropies. The weak uniaxial anisotropy changes slightly with T_S increasing. In contrast, the biaxial cubic anisotropy that arises from the improved crystal structure and increased biaxial stress upon thermal heating is negligibly small at $T_S \leq 300$ °C but increases considerably at $T_S > 300$ °C. Most importantly, we find that the increased $L2_1$ ordering degree would not reduce the biaxial cubic anisotropy. Our results facilitate the practical design of spintronic devices based on full-Heusler CFS thin films with controllable magnetic anisotropy.

ACKNOWLEDGMENTS

[1] H. C. Kandpal, G. H. Fecher, and C. Felser, Calculated electronic and magnetic properties of the half metallic, transition metal based Heusler compounds, J. Phys. D 40, 1507 (2007).

[2] R. A. de Groot, F. M. Mueller, P. G. van Engen, and K. H. J. Buschow, New Class of Materials: Half-Metallic Ferromagnets, Phys. Rev. Lett. 50, 2024 (1983).

[3] A. Hirohata, M. Kikuchi, N. Tezuka, K. Inomata, J. Claydon, Y. Xu, and G. Vanderlaan, Heusler alloy/semiconductor hybrid structures, Curr. Opin. Solid State Mater. Sci. 10, 93 (2006).

[4] M. Belmeguenai,, H. Tuzcuoglu, M. S. Gabor, T. Petrisor, C. Tiusan, D. Berling, F. Zighem, T. Chauveau, S. M. Cherif, and P. Moch, Co_2FeAl thin films grown on MgO substrates: Correlation between static, dynamic, and structural properties, Phys. Rev. B 87, 184431 (2013).

[5] I. Galanakis, P. H. Dederichs, and N. Papanikolaou, Slater-Pauling behavior and origin of the half-metallicity of the full-Heusler alloys, Phys. Rev. B 66, 174429 (2002).

[6] M. Meinert, J. M. Schmalhorst, M. Glas, G. Reiss, E. Arenholz, T. Bohnert, and K. Nielsch, Insights into the electronic structure of Co_2FeSi from x-ray magnetic linear dichroism, Phys. Rev. B 86, 054420 (2012).

[7] C. J. Palmstrøm, Heusler compounds and spintronics, Prog. Crystal Growth Charact. Mater. 62, 371 (2016).

[8] M. Oogane, M. Shinano, Y. Sakuraba, and Y. Ando, Tunnel magnetoresistance effect in magnetic tunnel junctions using epitaxial Heusler alloy electrode, J. Appl. Phys. 105, 07C903 (2009).

[9] N. Tezuka, N. Ikeda, F. Mitsuhashi, and S. Sugimoto, Improved tunnel magnetoresistance of magnetic tunnel junctions with Heusler $Co_2FeAl_{0.5}Si_{0.5}$ electrodes fabricated by molecular beam epitaxy, Appl. Phys. Lett. 94, 162504 (2009).

[10] H. X. Liu, T. Kawami, K. Moges, T. Uemura, M. Yamamoto, F. Y. Shi, and P. M. Voyles, Influence of film composition in quaternary Heusler alloy $Co_2(Mn, Fe)Si$ thin films on tunnelling magnetoresistance of $Co_2(Mn, Fe)Si/MgO$-based magnetic tunnel junctions, J. Phys. D 48, 164001 (2015).

[11] K. Yakushiji, K. Saito, S. Mitani, K. Takanashi, Y. K. Takahashi, and K. Hono, Current-perpendicular-to-plane magnetoresistance in epitaxial $Co_2MnSi/Cr/Co_2MnSi$ trilayers, Appl. Phys. Lett. 88, 222504 (2006).

[12] Y. K. Takahashi, A. Srinivasan, B. Varaprasad, A. Rajanikanth, N. Hase, T. M. Nakatani, S. Kasai, T. Furubayashi, and K. Hono, Large magnetoresistance in current-perpendicular-to-plane pseudospin valve using a $Co_2Fe(Ge_{0.5}Ga_{0.5})$ Heusler alloy, Appl. Phys. Lett. 98, 152501 (2011).

[13] Y. Sakuraba, M. Ueda, Y. Miura, K. Sato, S. Bosu, K. Saito, M. Shirai, T. J. Konno, and K. Takanashi, Extensive study of giant magnetoresistance properties in half-metallic $Co_2(Fe, Mn)Si$ based devices, Appl. Phys. Lett. 101, 252408 (2012).

[14] T. Akiho, J. H. Shan, H. X. Liu, K. Matsuda, M. Yamamoto, and T. Uemura, Electrical injection of spin-polarized electrons and electrical detection of dynamic nuclear polarization using a Heusler alloy spin source, Phys. Rev. B 87, 235205 (2013).

[15] P. Bruski, Y. Manzke, R. Farshchi, O. Brandt, J. Herfort, and M. Ramsteiner, All-electrical spin injection and detection in the $Co_2FeSi/GaAs$ hybrid system in the local and non-local configuration, Appl. Phys. Lett. 103, 052406 (2013).

[16] Y. Ebina, T. Akiho, H. X. Liu, M. Yamamoto, and T. Uemura, Effect of CoFe insertion in $Co_2MnSi/CoFe/n$-GaAs junctions on spin injection properties, Appl. Phys. Lett. 104, 172405 (2014).

[17] S. Mangin, D. Ravelosona, J. A. Katine, M. J. Carey, B. D. Terris, and E. E. Fullerton, Current-inducedmagnetization reversal in nanopillars with perpendicular anisotropy, Nat. Mater. **5,** 210 (2006).

[18] H. Sukegawa, Z. C. Wen, S. Kasai, K. Inomata, and S. Mitani, Spin transfer torque switching and perpendicular magnetic anisotropu in full Heusler alloy Co_2FeAl-based tunnel junctions, SPIN **4,** 1440023 (2014).

[19] Y. Takamura, R. Nakane, and S. Sugahara, Analysis of $L2_1$-ordering in full-Heusler Co_2FeSi alloy thin films formed by rapid thermal annealing, J. Appl. Phys. **105,** 07B109 (2009).

[20] M. Zhai, S. Ye, Z. Xia, F. Liu, C. Qi, X. Shi, and G. Wang, Local lattice distortion effect on the magnetic ordering of the Heusler alloy $Co_2FeAl_{0.5}Si_{0.5}$ film, J. Supercond. Novel Magn. **27,** 1861 (2014).

[21] M. Belmeguenai, H. Tuzcuoglu, M. S. Gabor, T. Petrisor, C. Tiusan, F. Zighem, S. M. Chérif, and P. Moch, Co_2FeAl Heusler thin films grown on Si and MgO substrates: Annealing temperature effect, J. Appl. Phys. **115,** 043918 (2014).

[22] Y. Liu, L. R. Shelford, V. V. Kruglyak, R. J. Hicken, Y. Sakuraba, M. Oogane, and Y. Ando, Optically induced magnetization dynamics and variation of damping parameter in epitaxial Co_2MnSi Heusler alloy films, Phys. Rev. B **81,** 094402 (2010).

[23] M. S. Gabor, M. Belmeguenai, T. Petrisor, C. Ulhaq-Bouillet, S. Colis, and C. Tiusan, Correlations between structural, electronic transport, and magnetic properties of $Co_2FeAl_{0.5}Si_{0.5}$ Heusler alloy epitaxial thin films, Phys. Rev. B **92,** 054433 (2015).

[24] Y. Cui, J. Lu, S. Schäfer, B. Khodadadi, T. Mewes, M. Osofsky, and S. A. Wolf, Magnetic damping and spin polarization of highly ordered $B2$ Co_2FeAl thin films, J. Appl. Phys. **116,** 073902 (2014).

[25] S. Trudel, O. Gaier, J. Hamrle, and B. Hillebrands, Magnetic anisotropy, exchange and damping in cobalt-based full-Heusler compounds: an experimental review, J. Phys. D **43,** 193001 (2010).

[26] Y. Miura, K. Nagao, and M. Shirai, Atomic disorder effects on half-metallicity of the full-Heusler alloys $Co_2(Cr_{1-x}Fe_x)Al$: A first-principles study, Phys. Rev. B **69,** 144413 (2004).

[27] R. Yilgin, M. Oogane, S. Yakata, Y. Ando, and T. Miyazaki, Intrinsic Gilbert damping constant in Co_2MnAl Heusler alloy films, IEEE Trans. Magn. **41,** 2799 (2005).

[28] M. Oogane, T. Kubota, H. Naganuma, and Y. Ando, Magnetic damping constant in Co-based full Heusler alloy epitaxial films, J. Phys. D **48,** 164012 (2015).

[29] M. Belmeguenai, F. Zighem, T. Chauveau, D. Faurie, Y. Roussigné, S. M. Chérif, P. Moch, K. Westerholt, and P. Monod, Structural, static and dynamic magnetic properties of thin films on a sapphire-plane substrate, J. Appl. Phys. **108,** 063926 (2010).

[30] M. Kallmayer, H. Schneider, G. Jakob, H. J. Elmers, B. Balke, and S. Cramm, Interface magnetization of ultrathin epitaxial $Co_2FeSi(110)/Al_2O_3$ films, J. Phys. D **40,** 1552 (2007).

[31] T. Ambrose, J. J. Krebs, and G. A. Prinz, Epitaxial growth and magnetic properties of single-crystal Co_2MnGe Heusler alloy films on GaAs (001), Appl. Phys. Lett. **76,** 3280 (2000).

[32] W. Wang, H. Sukegawa, R. Shan, T. Furubayashi, and K. Inomata, Preparation and characterization of highly $L2_1$-ordered full-Heusler alloy $Co_2FeAl_{0.5}Si_{0.5}$ thin films for spintronics device applications, Appl. Phys. Lett. **92,** 221912 (2008).

[33] H. C. Yuan, S. H. Nie, T. P. Ma, Z. Zhang, Z. Zheng, Z. H. Chen, Y. Z. Wu, J. H. Zhao, H. B. Zhao, and L. Y. Chen, Different temperature scaling of strain-induced magneto-crystalline anisotropy and Gilbert damping in Co_2FeAl film epitaxied on GaAs, Appl. Phys. Lett. **105,** 072413 (2014).

[34] S. Kawagishi, T. Uemura, Y. Imai, K. I. Matsuda, and M. Yamamoto, Structural, magnetic, and electrical properties of $Co_2MnSi/MgO/n$-GaAs tunnel junctions, J. Appl. Phys. **103,** 07A703 (2008).

[35] T. Yano, T. Uemura, K. i. Matsuda, and M. Yamamoto, Effect of a MgO interlayer on the structural and magnetic properties of $Co_2Cr_{0.6}Fe_{0.4}Al$ thin films epitaxially grown on GaAs substrates, J. Appl. Phys. **101,** 063904 (2007).

[36] S. Yamada, K. Hamaya, K. Yamamoto, T. Murakami, K. Mibu, and M. Miyao, Significant growth-temperature dependence of ferromagnetic properties for $Co_2FeSi/Si(111)$ prepared by low-temperature molecular beam epitaxy, Appl. Phys. Lett. **96,** 082511 (2010).

[37] M. S. Gabor, T. Petrisor, C. Tiusan, M. Hehn, and T. Petrisor, Magnetic and structural anisotropies of Co_2FeAl Heusler alloy epitaxial thin films, Phys. Rev. B **84,** 134413 (2011).

[38] S. Trudel, G. Wolf, J. Hamrle, B. Hillebrands, P. Klaer, M. Kallmayer, H. J. Elmers, H. Sukegawa, W. Wang, and K. Inomata, Effect of annealing on $Co_2FeAl_{0.5}Si_{0.5}$ thin films: A magneto-optical and x-ray absorption study, Phys. Rev. B **83,** 104412 (2011).

[39] O. Gaier, J. Hamrle, S. J. Hermsdoerfer, H. Schultheiß, B. Hillebrands, Y. Sakuraba, M. Oogane, and Y. Ando, Influence of the $L2_1$ ordering degree on the magnetic properties of Co_2MnSi Heusler films, J. Appl. Phys. **103,** 103910 (2008).

[40] D. Wu, Z. Zhang, L. Li, Z. Zhang, H. B. Zhao, J. Wang, B. Ma, and Q. Y. Jin, Perpendicular magnetic anisotropy and magnetization dynamics in oxidized CoFeAl films, Sci. Rep. **5,** 12352 (2015).

[41] B. Balke, S. Wurmehl, G. H. Fecher, C. Felser, and J. Kubler, Rational design of new materials for spintronics: Co_2FeZ (Z = Al, Ga, Si, Ge), Sci. Technol. Adv. Mater. **9,** 014102 (2008).

[42] A. L. Patterson, The Scherrer formula for x-ray particle size determination, Phys. Rev. **56,** 978 (1939).

[43] Y. Takamura, T. Sakurai, R. Nakane, Y. Shuto, and S. Sugahara, Epitaxial germanidation of full-Heusler Co_2FeGe alloy thin films formed by rapid thermal annealing, J. Appl. Phys. **109,** 07B768 (2011).

[44] K. Ziebeck and P. Webster, A neutron diffraction and magnetization study of Heusler alloys containing Co and Zr, Hf, V or Nb, J. Phys. Chem. Solids **35,** 1 (1974).

[45] M. Belmeguenai, F. Zighem, Y. Roussigné, S. M. Chérif, P. Moch, K. Westerholt, G. Woltersdorf, and G. Bayreuther, Microstrip line ferromagnetic resonance and Brillouin light scattering investigations of magnetic properties of Co_2MnGe Heusler thin films, Phys. Rev. B **79,** 024419 (2009).

[46] E. C. Stoner and E. Wohlfarth, A mechanism of magnetic hysteresis in heterogeneous alloys, Phil. Trans. R. Soc. A **240**, 599 (1948).

[47] S. Wurmehl, G. H. Fecher, H. C. Kandpal, V. Ksenofontov, C. Felser, and H.-J. Lin, Investigation of Co_2FeSi: The Heusler compound with highest Curie temperature and magnetic moment, Appl. Phys. Lett. **88**, 032503 (2006).

[48] M. Emmel *et al.*, Electronic properties of Co_2FeSi investigated by x-ray magnetic linear dichroism, J. Magn. Magn. Mater. **368**, 364 (2014).

[49] B. S. Chun *et al.*, Structural and magnetic properties of epitaxial Co_2FeAl films grown on MgO substrates for different growth temperatures, Acta Mater. **60**, 6714 (2012).

[50] F. Bianco, P. Bouchon, M. Sousa, G. Salis, and S. F. Alvarado, Enhanced uniaxial magnetic anisotropy in $Fe_{31}Co_{69}$ thin films on GaAs(001), J. Appl. Phys. **104**, 083901 (2008).

[51] T. J. Klemmer, K. A. Ellis, L. H. Chen, B. van Dover, and S. Jin, Ultrahigh frequency permeability of sputtered Fe–Co–B thin films, J. Appl. Phys. **87**, 830 (2000).

[52] K. Ozawa, T. Yanada, H. Masuya, M. Sato, S. Ishio, and M. Takahashi, Oblique incidence effects in evaporated iron thin films, J. Magn. Magn. Mater. **35**, 289 (1983).

[53] S. Jo, Y. Choi, and S. Ryu, Magnetic anisotropy of sputtered FeN films due to anisotropic columnar growth of grains, IEEE Trans. Magn. **33**, 3634 (1997).

[54] S. Pan, S. Mondal, T. Seki, K. Takanashi, and A. Barman, Influence of thickness-dependent structural evolution on ultrafast magnetization dynamics in $Co_2Fe_{0.4}Mn_{0.6}Si$ Heusler alloy thin films, Phys. Rev. B **94**, 184417 (2016).

[55] S. Qiao, W. Yan, S. Nie, J. Zhao, and X. Zhang, The in-plane anisotropic magnetic damping of ultrathin epitaxial Co_2FeAl film, AIP Adv. **5**, 087170 (2015).